ELSEVIER

Journal of Nuclear Materials 295 (2001) 109–120

journal of nuclear materials

www.elsevier.nl/locate/jnucmat

Hydrogen concentrations near cracks in target materials for high-power spallation neutron sources ☆

H. Rauh [a,*], H. Ullmaier [b]

[a] *Institut für Materialwissenschaft, Technische Universität Darmstadt, Petersenstrasse 23, D-64287 Darmstadt, Germany*
[b] *Institut für Festkörperforschung, Forschungszentrum Jülich, Postfach 1913, D-52425 Jülich, Germany*

Received 4 October 2000; accepted 21 December 2000

Abstract

Materials in the target region of spallation neutron sources which are exposed, or are close to the proton beam suffer from high rates of displacement damage and the production of foreign elements, particularly hydrogen and helium isotopes. Whilst some results on the effect of helium are now available, there is little information on the potential influence of hydrogen in the environment of a spallation source. We therefore investigate theoretically the establishment of hydrogen background concentrations and their enhancement near microcracks in proton-irradiated plates of ferritic/martensitic steel and tantalum, respectively, for the conditions of the envisaged 5 MW European Spallation Source (ESS). A comparison of the predicted hydrogen concentrations with empirical threshold concentrations for hydrogen embrittlement and hydride formation indicates that the use of ferritic/martensitic steels for water-cooled windows may be problematic, although these materials remain good candidates for the mercury container. Tantalum as a prospective material for the solid target option of ESS is not expected to undergo hydrogen degradation.

1. Introduction

In spallation sources, the neutrons used as probes for condensed matter research are generated by high-energy protons which induce spallation of the nuclei of heavy-metal targets. Apart from having higher efficiencies for neutron production than fission reactors, spallation sources can relatively easily deliver neutron pulses of lengths in the range of microseconds through the imposition of a time structure on the proton beam. This not only increases the peak intensities but also allows time-of-flight measurements to be carried out, making for many applications more efficient use of the neutrons than cw sources. A brief review of accelerator concepts capable of providing proton beams of suitable energy, intensity, pulse and cycle length can be found in [1]. The recently completed feasibility study for the construction of the high-power European Spallation Source (ESS) proposes an average proton beam power per pulsing cycle of 5 MW [2]. Because of the very high beam intensity, radiation damage will play a crucial role for the lifetime of materials in the target region of this source [3].

Radiation damage in metals is the consequence of two elementary types of interaction of the irradiating particles with the nuclei of the respective material: (i) transfer of recoil energy to lattice atoms, leading to their displacement, i.e. to the creation of vacancies and self-interstitial defects; (ii) nuclear reactions, giving rise to the production of foreign elements. Radiation effects relevant to fission reactor technology, viz. hardening, in-pile creep and swelling, are mainly due to displacement damage. In nuclear systems involving particles of very high energy, however, nuclear reactions may take over the dominant part. For example, the 14 MeV neutrons, which will bombard the metallic near-plasma components of envisaged fusion reactors,

☆ Dedicated to Professor R. Bullough, F.R.S. on the occasion of his 70th birthday.

* Corresponding author. Tel.: +49-6151 16 3374; fax: +49-6151 16 6038.
E-mail address: hera@hrzpub.tu-darmstadt.de (H. Rauh).

0022-3115/01/$ - see front matter
PII: S0022-3115(01)00430-5

have large cross-sections for (n,p)- and (n,α)-reactions, yielding high production rates of hydrogen and helium isotopes. At elevated temperatures, helium forms bubbles which may cause severe embrittlement [4]. In target materials for high-power spallation sources, even higher production rates will be brought forth by the incident protons and the generated neutrons having energies around 1 GeV. Since such targets are expected to operate at relatively low temperatures [2], helium will be virtually immobile, and bubble formation hence strongly retarded. On the other hand, hydrogen diffusion will also be slowed down, resulting in the build-up of high hydrogen concentrations which may induce hydrogen embrittlement. This problem appears to be most serious for hydride-forming metals like zirconium or tantalum; it is also important, however, for ferritic/martensitic steels, being prospective materials for the components of liquid metal targets [5]. Estimating the hydrogen concentrations likely to prevail in structural plates of steel and tantalum subject to the conditions of ESS therefore is the main focus of the present investigation, with particular strength on an analysis of the enhancement of these concentrations due to stress-driven hydrogen accumulation [6–12] near microcracks, which exist in every engineering material and here constitute the most important type of flaw.

Proceeding from the data anticipated for the proton and neutron fluxes as well as from the appropriate values of the cross-sections for proton- and neutron-induced reactions, we first establish in Section 2 the expected hydrogen production rate. Referring to the steady-state pulsing regime, we then determine in Section 3 the hydrogen background concentration in steel and tantalum plates, allowing for possible contamination of their surfaces. In addition to irradiation-induced hydrogen production, we also contemplate hydrogen supply from an external hydrogen atmosphere. By adopting a simple embedding approach for an isotropic elastic/ideally plastic continuum, we estimate in Section 4 the enhancement of the hydrogen background concentration near microcracks, whose stress-field characteristic depends crucially on the specific situation, e.g. through the applied load, the actual flow stress, and the partial pressure of their internal hydrogen atmosphere. Since we wish to appraise upper bounds, we refer to microcracks under mode I loading in the centre of the plates, assuming local equilibrium between these cracks and the hydrogen solution surrounding them, and dwelling on their strongest interaction with atomically dissolved hydrogen. Finally, we discuss in Section 5 the maximum hydrogen concentrations predicted by our analysis in the light of critical values for detrimental hydrogen effects known from the literature and assess implications for the performance of structural materials in the environment of ESS.

2. Hydrogen production rate

The average beam power per pulsing cycle of 5 MW, derived from a periodic sequence of rectangular pulses with the pulse length $t_p = 1$ μs and the cycle length $T_p = 20$ ms, as envisaged for ESS, will be achieved by a 3.75 mA current of 1.33 GeV protons. An optimum beam would have an elliptic cross-section of dimension 200 mm × 60 mm and a parabolic intensity distribution, corresponding to an average current density of 0.75 A m^{-2}, i.e. to an average proton flux $\Phi_p = 4.7 \times 10^{18}$ m^{-2} s^{-1}, in the centre of the beam. The most critical target components, regarding radiation damage and mechanical stress, are the beam entry window and the target material close to it. Nuclear calculations suggest that, in addition to the proton flux, these regions will also be exposed to an average neutron flux $\Phi_n = 1.0 \times 10^{18}$ m^{-2} s^{-1}, with neutron energies up to 1.33 GeV [13].

The average hydrogen and helium production rates per atom and pulsing cycle are determined by the average proton and neutron fluxes in conjunction with the appropriate reaction cross-sections, σ_H and σ_{He}. Typical values of the latter for 0.75 GeV protons, showing the dependence on the atomic number Z of the target material, are presented in Fig. 1. Recent studies confirm these data and indicate that σ_{He} follows an approximately linear dependence on the particle energy in the range between 0.75 and 1.33 GeV [15]. Assuming σ_H varies linearly too gives σ_H at the higher energy equal to about 1.5 times the respective value at the lower energy, taking account of the reaction cross-sections of all three kinds of hydrogen isotopes. This estimate, together with the data of Fig. 1, renders a hydrogen reaction cross-section $\sigma_H = (1.6 \pm 0.3) \times 10^{-27}$ m^2 for iron ($Z = 26$) or

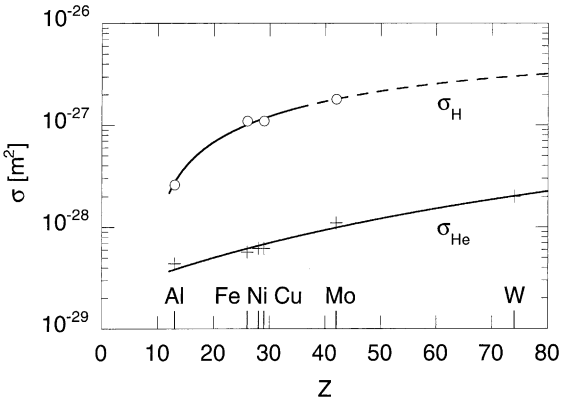

Fig. 1. Hydrogen and helium reaction cross-sections for 0.75 GeV protons, σ_H and σ_{He}, with varying atomic number Z of the target material [14]. The full lines drawn through the data points and the (extrapolated) broken line serve as eye guides only.

steel and $\sigma_H = (4.5 \pm 0.9) \times 10^{-27}$ m^2 for tantalum ($Z = 73$) in the case of 1.33 GeV particles. Since proton- and neutron-induced reactions are comparable at such a high energy, these values can be expected to apply to either type of the projectiles. Multiplying the sum of Φ_p and Φ_n with σ_H thus yields the average hydrogen production rate per atom and pulsing cycle $P = (9.1 \pm 1.7) \times 10^{-9}$ s^{-1} for steel and $P = (2.56 \pm 0.51) \times 10^{-8}$ s^{-1} for tantalum.

3. Hydrogen background concentration

We consider an infinitely extended metallic plate of thickness $2d$ subject to high-energy particle irradiation of the pulsed form outlined before. If z denotes a cartesian axis normal to the surfaces (with its origin at the centre) of the plate, $z = 0$, and t means time, then the average fractional hydrogen concentration per pulsing cycle $c(z,t)$ inside the plate, $-d < z < d$, satisfies the continuity equation

$$D_{\text{eff}} \frac{\partial^2 c}{\partial z^2} + P = \frac{\partial c}{\partial t} \tag{1}$$

with an effective diffusion coefficient, D_{eff}, describing hydrogen diffusion in the presence of possible traps [16], which certainly defines a reasonable approach if, as assumed here, the shortest distance between traps is much smaller than the thickness of the plate. Fig. 2 shows experimental values of this coefficient relating to steel and tantalum, respectively, for a range of inverse absolute temperatures. In the absence of an external hydrogen atmosphere, i.e. for zero hydrogen partial pressure outside the plate, $p_{\text{ext}} = 0$, the relevant boundary conditions are

$$-D_{\text{eff}} \frac{\partial c}{\partial z} = \pm \upsilon c \quad \text{at } z = \pm d, \tag{2}$$

implying continuity of the hydrogen current density, with υ expressing the velocity of hydrogen transfer across the surfaces of the plate [21].

In the steady-state pulsing regime, strictly attained as $t \to \infty$, the average fractional hydrogen concentration reads

$$c(z,\infty) = \frac{Pd^2}{2D_{\text{eff}}} \left(1 + \frac{2l}{d} - \left(\frac{z}{d}\right)^2\right), \tag{3}$$

where $l = D_{\text{eff}}/\upsilon$ represents the transfer length associated with hydrogen loss through the surfaces of the plate [21]: instantaneous outflow, like for ideal ('clean') surfaces, is typified by $l = 0$, whereas inhibited outflow, like for real ('contaminated') surfaces, is characterized by $l > 0$. The dimensionless ratio l/d, known as the inverse Hobson number [22,23], thus measures the diffusion resistance of the surfaces of the plate relative to that of the material bulk. For each value of this number, the parabolic concentration profile, Eq. (3), adopts its maximum,

$$c_0 = \frac{Pd^2}{2D_{\text{eff}}} \left(1 + \frac{2l}{d}\right), \tag{4}$$

in the centre of the plate. Fig. 3 portrays the steady-state average fractional hydrogen concentration given by Eq. (4), i.e. the fractional hydrogen background concentration at $z = 0$, as a function of the plate half-thickness, in the case of steel and tantalum, respectively, at two extreme temperatures and for two extreme values of the transfer length; conditions of the surface state which should safely encompass those expected to prevail in the target region of ESS. We note a reduction of the maximum hydrogen background concentration at the higher temperature and a rise in the presence of surface contamination, most pronounced for small values of the half-thickness of the plate.

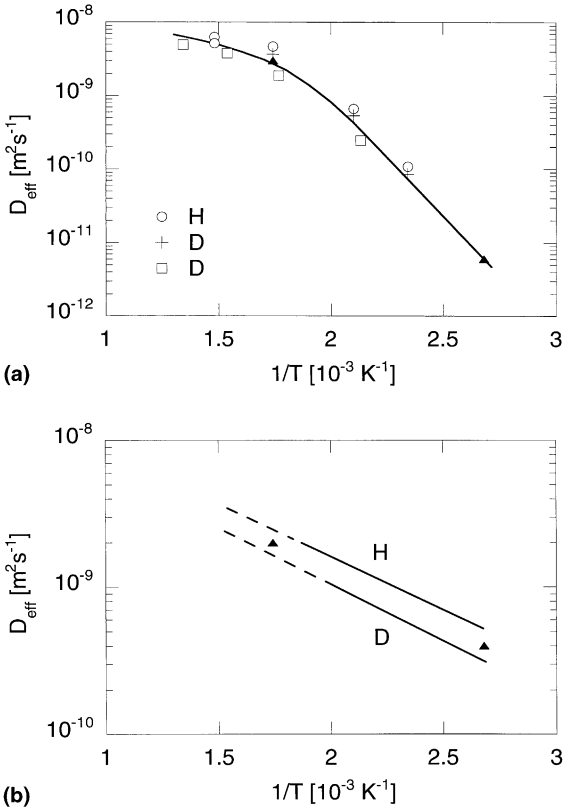

Fig. 2. Effective diffusion coefficient of hydrogen isotopes, D_{eff}, with varying inverse absolute temperature $1/T$ in (a) steel [17,18] and (b) tantalum [19]. The strong decrease at low temperature of the hydrogen diffusivity in steel is attributed to hydrogen trapping at defects [20] contained abundantly in this material. The solid triangles denote the data used in the present work.

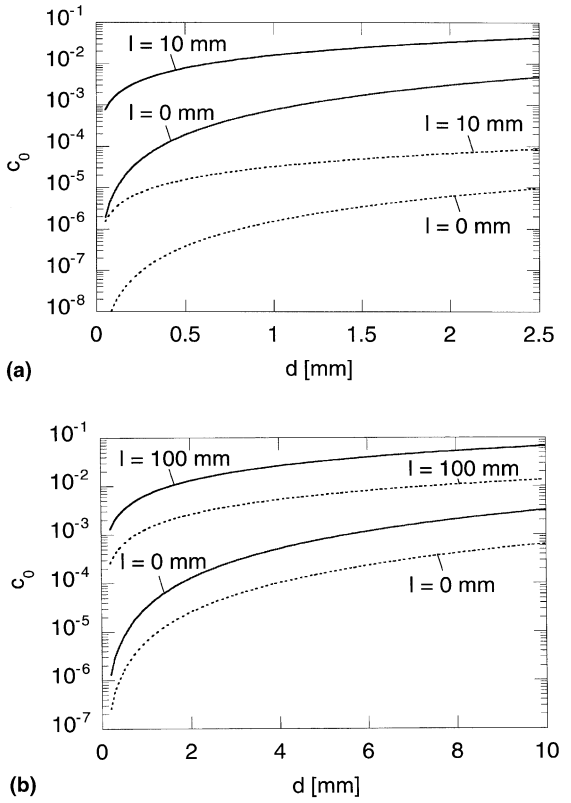

Fig. 3. Fractional hydrogen background concentration in the centre of a plate, c_0, as a function of the plate half-thickness d, at a temperature ϑ of 100°C (full lines) and 300°C (dotted lines) for two different values of the transfer length l identified on the curves, in the case of (a) steel and (b) tantalum, obtained using the data in Table 1.

For all practical purposes, the duration of the build-up of the steady-state average fractional hydrogen concentration from initially zero hydrogen concentration is determined by the relaxation time of the fundamental mode of the appropriate eigenfunction expansion of the complete solution to Eqs. (1) and (2), $\tau_r = 1/\lambda^2 D_{\text{eff}}$, i.e. by the smallest (positive) root of the transcendental relation

$$\lambda l = \cot \lambda d, \tag{5}$$

whence

$$\tau_r \approx \begin{cases} \left(1+\dfrac{l}{d}\right)^2 \tau_0 & \text{if } \dfrac{l}{d} \ll 1, \\ \dfrac{\pi^2}{4}\left(\dfrac{1}{3}+\dfrac{l}{d}\right)\tau_0 & \text{if } \dfrac{l}{d} \gg 1, \end{cases} \tag{6}$$

with

$$\tau_0 = \frac{4d^2}{\pi^2 D_{\text{eff}}}. \tag{7}$$

The variation of this time with the inverse Hobson number, following from Eq. (5), is displayed in Fig. 4, again in the case of steel and tantalum, respectively, at the same temperatures and for two extreme values of the half-thickness of the plate. This reveals a decrease of the relaxation time at the higher temperature and an increase for the greater half-thickness of the plate, which is particularly distinct for large values of the inverse Hobson number. The fact that τ_r is always several orders of magnitude larger than T_p justifies our focussing on the timeindependent average, rather than on the actual time-dependent fractional hydrogen concentration in the steady-state pulsing regime. Formally, the periodic hydrogen concentration fluctuations in the centre of the plate, δc_0, with maxima of the order of PT_p due to pulsing of the beam, and the steady-state average hydrogen concentration, c_0, compare like $\delta c_0/c_0 \approx T_p/\tau_r$ in this regime and for ideally permeable surfaces. The actual hydrogen concentration here (and, a fortiori, for surfaces with restricted permeability) thus is quasi-static. A solution of the complete time-dependent problem

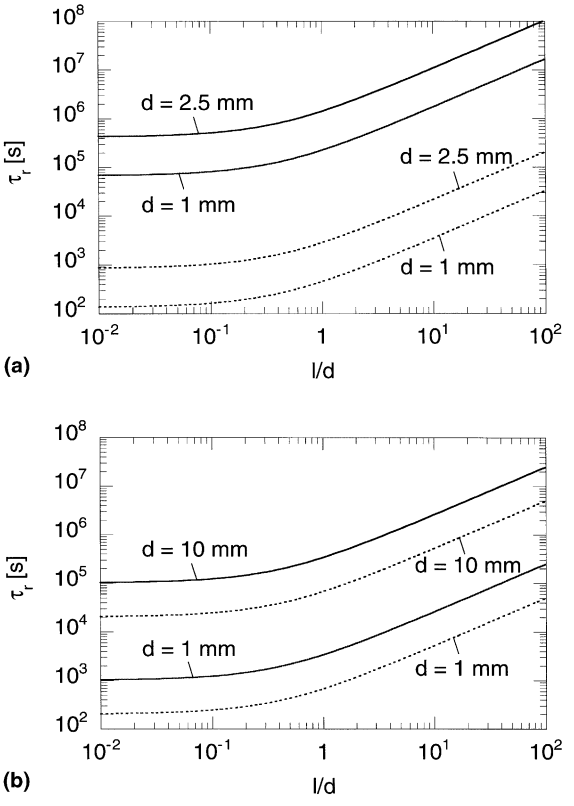

Fig. 4. Relaxation time, τ_r, as a function of the inverse Hobson number l/d, at a temperature ϑ of 100°C (full lines) and 300°C (dotted lines) for two different values of the plate half-thickness d identified on the curves, in the case of (a) steel and (b) tantalum, obtained using the data in Table 1.

Table 1
Physical data used in calculations

(a) *Steel*	
Hydrogen production rate	$P = 9.1 \times 10^{-9}$ s^{-1} (Section 2)
Hydrogen diffusion coefficient	$D_{\text{eff}}(100°\text{C}) = 6 \times 10^{-12}$ m^2 s^{-1} (Fig. 2(a))
	$D_{\text{eff}}(300°\text{C}) = 3 \times 10^{-9}$ m^2 s^{-1} (Fig. 2(a))
Hydrogen Sievert constant	$S(100°\text{C}) = 4.71 \times 10^{-8}$ Pa$^{-1/2}$ [18]
	$S(300°\text{C}) = 1.00 \times 10^{-8}$ Pa$^{-1/2}$ [18]
Tensile flow stress	$\sigma_{\text{F}}(100°\text{C}) = 800$ MPa
	$\sigma_{\text{F}}(300°\text{C}) = 650$ MPa
Hydrogen relaxation volume	$\Delta V = 3.3 \times 10^{-30}$ m^3 [24,25]
Poisson ratio	$\nu = 0.28$
Bulk modulus	$B = 164$ GPa
(b) *Tantalum*	
Hydrogen production rate	$P = 2.56 \times 10^{-8}$ s^{-1} (Section 2)
Hydrogen diffusion coefficient	$D_{\text{eff}}(100°\text{C}) = 4 \times 10^{-10}$ m^2 s^{-1} (Fig. 2(b))
	$D_{\text{eff}}(300°\text{C}) = 2 \times 10^{-9}$ m^2 s^{-1} (Fig. 2(b))
Hydrogen Sievert constant	$S(100°\text{C}) = 5.08 \times 10^{-3}$ Pa$^{-1/2}$ [26]
	$S(300°\text{C}) = 1.46 \times 10^{-4}$ Pa$^{-1/2}$ [26]
Tensile flow stress	$\sigma_{\text{F}}(100°\text{C}) = 980$ MPa
	$\sigma_{\text{F}}(300°\text{C}) = 700$ MPa
Hydrogen relaxation volume	$\Delta V = 2.77 \times 10^{-30}$ m^3 [26,27]
Poisson ratio	$\nu = 0.35$
Bulk modulus	$B = 193$ GPa

relating to the above situation can be deduced from the analysis in [28].

If the plate is exposed to an external hydrogen atmosphere of finite partial pressure, $p_{\text{ext}} > 0$, then the fractional hydrogen background concentration locally adopts the thermal equilibrium level, $\bar{c}_{\text{e}}$, at least. For atomically dissolved hydrogen in equilibrium with molecular hydrogen gas, this level is related to the partial pressure p and the absolute temperature T through the generalized Sievert law [29]

$$\bar{c}_{\text{e}} = S\sqrt{f(p,T)p}, \tag{8}$$

taking real gas behaviour into account. S denotes the Sievert constant (assumed, for simplicity, to be independent of concentration) and $f(p,T)$ the fugacity coefficient defined as

$$f(p,T) = \exp\left(\int_0^p \left(\frac{V(p',T)}{k_{\text{B}}T} - \frac{1}{p'}\right) \mathrm{d}p'\right) \tag{9}$$

with the Boltzmann constant k_{B}, and the pressure and temperature dependence of the volume per hydrogen molecule V (which is uniquely determined in the pure gaseous phase) according to the chosen hydrogen gas equation of state. We note the limit of ideal gas behaviour as p approaches zero,

$$\lim_{p\to 0} f(p,T) = 1, \tag{10}$$

irrespective of T. In practice, virtually ideal gas behaviour, $f(p,T) \approx 1$, prevails even for $0 < p \ll p_{\text{c}}$, provided that $T \gg T_{\text{c}} > 0$, where p_{c} is the critical partial pressure and T_{c} the critical absolute temperature. Experiments with molecular hydrogen gas yield $p_{\text{c}} = 1.3$ MPa and $T_{\text{c}} = 33.2$ K [30].

The threshold hydrogen partial pressure $p = p^*_{\text{ext}}$ for which $\bar{c}_{\text{e}} = c_0$, i.e. when the thermal equilibrium concentration of dissolved hydrogen equals the fractional hydrogen background concentration in the centre of the plate, follows as a self-consistent solution of Eqs. (8) and (9) with Eq. (4) at each given temperature. We evaluate Eq. (9) on the basis of the Beattie–Bridgeman equation of state [31] and parameter values reported in [30], deemed to provide the most adequate representation available for molecular hydrogen gas [29]. The variation with the plate half-thickness of the threshold hydrogen partial pressure is illustrated in Fig. 5 in the case of steel and tantalum, respectively, at two extreme temperatures and again for two extreme values of the transfer length. Whilst this pressure increases for both steel and tantalum when surface barriers are present, it falls at the higher temperature in the case of steel and rises at the higher temperature in the case of tantalum, most markedly for small values of the half-thickness of the plate. Because of the very low solubility of hydrogen in steel, the threshold hydrogen partial pressure predicted at the lower temperature and for the greater transfer length is so high that it will probably never be attained in practice. By contrast, because of the very high solubility of hydrogen in tantalum, the threshold hydrogen partial pressure anticipated here is always well below normal level, and hence may easily be reached; an external

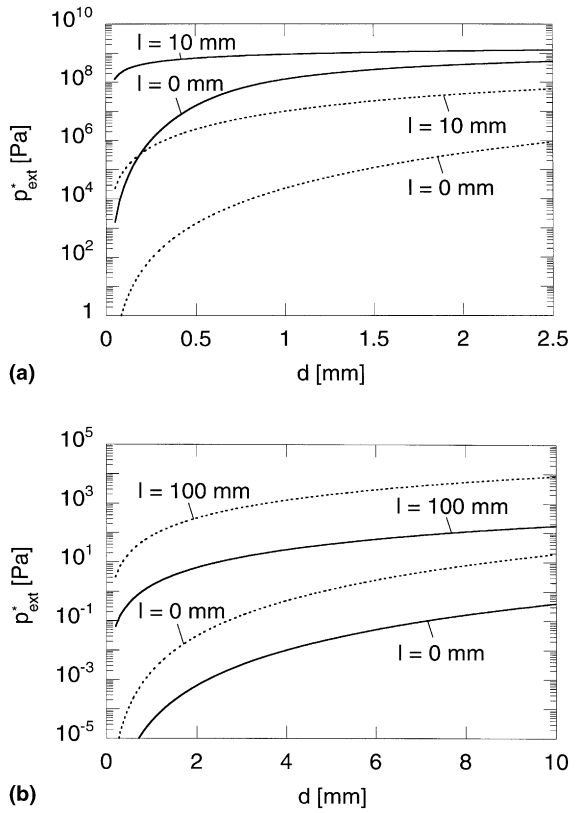

Fig. 5. Threshold partial pressure of an external hydrogen atmosphere, p^*_{ext}, as a function of the plate half-thickness d, at a temperature ϑ of 100°C (full lines) and 300°C (dotted lines) for two different values of the transfer length l identified on the curves, in the case of (a) steel and (b) tantalum, obtained using the data in Table 1.

hydrogen atmosphere may therefore enhance the concentration of dissolved hydrogen appreciably.

The foregoing considerations, by assumption, only apply to the situation of *molecular* hydrogen in contact with these materials. If the external atmosphere involves hydrogen in *atomic* or *ionized* form, i.e. as H, H^+ or H_2^+, levels of dissolved hydrogen even higher than the maximum fractional hydrogen background concentration due to irradiation-induced hydrogen production can be achieved [32,33]. This 'superpermeation' is sensitive to a variety of parameters which are difficult to quantify, and hence introduce large uncertainties into the assessment of hydrogen effects. Substances containing hydrogen (e.g. in molecular form, water or methane) should therefore be avoided in the highly ionizing environment of a spallation neutron source. If indispensable, as for neutron moderation or cooling, in situ experiments under realistic conditions are necessary in order to obtain trustworthy information.

4. Hydrogen concentration near a crack

In order to study the local enhancement of the maximum hydrogen background concentration due to stress-driven hydrogen accumulation, we consider a straight microcrack of length $2a$, embedded in the centre of the plate and surrounded by a hydrogen solution of fractional concentration c_0, modelling the plate as an isotropic elastic/ideally plastic continuum and adopting the extreme case of mode I loading of the crack by an external tensile stress σ_{ext} perpendicular to the crack-plane, as depicted in Fig. 6(a). The length of the crack is

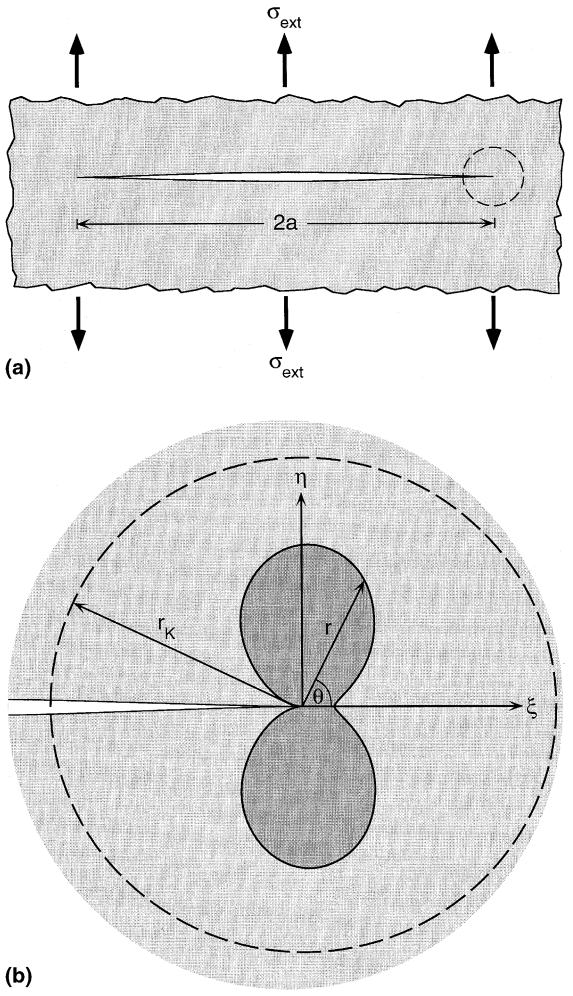

Fig. 6. (a) Microcrack of length $2a$, with an internal hydrogen atmosphere, in an isotropic elastic/ideally plastic continuum (light shading) under mode I loading by an external tensile stress σ_{ext} (bold arrows) perpendicular to the crack-plane; (b) enlargement of the near-field region of radius r_K around the (right) end of the crack, with its tip occupying the ζ-axis of a local cartesian system ξ, η, ζ. The plastic zone (dark shading; size not to scale!) drawn for the Poisson ratio $\nu = 0.3$ and the definition of cylindrical polar coordinates (r, θ) are indicated.

supposed to be much smaller than the thickness of the plate, whence plane-strain conditions can be assumed for which, using local cylindrical polar coordinates (r, θ) with their origin at the (right) crack-tip, the principal components of the tensor of elastic stress σ in the near-field region of radius r_K *outside* the plastic zone, $r_p(\theta) < r < r_K \ll a$, $-\pi < \theta < \pi$, read [34]

$$\begin{Bmatrix} \sigma_1 \\ \sigma_2 \\ \sigma_3 \end{Bmatrix} = \frac{K_I}{\sqrt{2\pi r}} \cos\frac{\theta}{2} \begin{Bmatrix} 1+\sin\theta/2 \\ 1-\sin\theta/2 \\ 2\nu \end{Bmatrix}. \tag{11}$$

Here, ν denotes the Poisson ratio and K_I the stress-intensity factor given by

$$K_I = (\sigma_{ext} + p_{int})\sqrt{\pi a}, \tag{12}$$

where p_{int} means the partial pressure of an internal atmosphere of molecular hydrogen gas in local equilibrium with atomically dissolved hydrogen encompassing the crack. Confining ourselves to small-scale yielding of the continuum with uniaxial tensile flow stress σ_F, when $\sigma_{ext} + p_{int} \ll \sigma_F$, we estimate the shape of the plastic zone by requiring that along its contour the components, Eq. (11), satisfy the von Mises yield criterion [35]

$$(\sigma_1 - \sigma_2)^2 + (\sigma_2 - \sigma_3)^2 + (\sigma_3 - \sigma_1)^2 = 2\sigma_F^2. \tag{13}$$

This furnishes the contour representation

$$r_p(\theta) = \frac{K_I^2}{2\pi\sigma_F^2} \cos^2\frac{\theta}{2} \left((1-2\nu)^2 + 3\sin^2\frac{\theta}{2} \right) \tag{14}$$

exhibiting the lateral extent of the plastic zone at $\theta = 0$,

$$r_p^* = \frac{1}{2\pi} \left((1-2\nu)\frac{K_I}{\sigma_F} \right)^2. \tag{15}$$

The near-field region and the plastic zone of the crack are illustrated in Fig. 6(b).

For present purposes, we characterize a hydrogen atom dissolved in steel or tantalum by its (isotropic) contribution to the dipole force tensor, F_0, constructed from the hydrogen Kanzaki forces and the perfect lattice sites, which describes lattice distortions due to the hydrogen impurity alone [36]. The energy of the associated (long-range) paraelastic, or size interaction between the hydrogen atom and the crack-tip stress field can then be put as

$$W = -\frac{1}{3}(\mathrm{tr}\,\sigma)\Delta V, \tag{16}$$

where the (positive) relaxation volume ΔV, originating from the strain field around the hydrogen defect and the action of image forces due to the surfaces of the plate, is related to F_0 via Hooke's law, $\Delta V = (\mathrm{tr}\,F_0)/3B$, with the bulk modulus B. Employing the components, Eq. (11), in Eq. (16) renders the explicit result

$$W = -\sqrt{\frac{2}{9\pi r}}(1+\nu)K_I\Delta V \cos\frac{\theta}{2}, \tag{17}$$

which has also been derived before using an alternative approach [10]. The energy specified in Eq. (17) adopts its minimum,

$$W_{min} = -\frac{2}{3}\left(\frac{1+\nu}{1-2\nu}\right)\sigma_F\Delta V, \tag{18}$$

on the contour of the plastic zone in the crack-plane ahead of the crack-tip, i.e. for $r = r_p^*$, $\theta = 0$. Eq. (18), obtained from Eq. (17) by virtue of Eq. (15), is remarkable as it reveals the dependence of this minimum on the flow, rather than on the external stress through the stress-intensity factor itself.

To be exact, a hydrogen impurity dissolved in either of the materials considered here is further characterized by an (anisotropic) contribution to the dipole force tensor, F_1, made up of the tensors of the hydrogen elastic polarizability and the crack-tip elastic stress, which describes modifications of the hydrogen Kanzaki forces due to the prestrained lattice in the presence of the crack [36]. This contribution gives rise to the energy of the (short-range) diaelastic, or inhomogeneity interaction and tends to mitigate the size interaction in strength. Its strict representation would require the use of cubic, rather than isotropic elasticity. An estimate based on the available data of the hydrogen elastic polarizability [36,37], the physical data of Table 1 and the components of the tensor of elastic stress, Eq. (11), however shows, in accord with the findings in [10], that the energy of the inhomogeneity interaction in the near-field region outside the plastic zone right up to $r = r_p^*$, $\theta = 0$ amounts to merely a few percent of the absolute magnitude of the minimum energy of the size interaction, Eq. (18), at best, considering all relevant conditions of flow and external stress, and thus is disregarded here. Practically, the effect of the inhomogeneity interaction is completely masked by the uncertainty of the size interaction arising from the inaccuracy associated with quantitative determinations of the paraelastic contribution to the dipole force tensor or, respectively, the relaxation volume of the hydrogen defect.

Clearly, owing to the relaxation of stress, the energy of the interaction between a hydrogen atom and the crack-tip stress field *inside* the plastic zone, $0 \leqslant r < r_p(\theta)$, $-\pi < \theta < \pi$, which must be continuous across the contour of this zone, will fall nowhere below the minimum level remarked on above [35]. Eq. (18) therefore represents the strongest interaction indeed.

Making use of the Bragg–Williams model for concentrated solutions of mutually non-interacting hydrogen atoms, in which site competition through short-range repulsions is accounted for implicitly by ensuring that no two solute atoms can occupy the same site, the maximum fractional hydrogen concentration due to

stress-driven hydrogen accumulation in front of the crack-tips follows from the Fermi–Dirac distribution [38]

$$c_{\max} = 1 \Big/ \left\{ \exp\left(\frac{W_{\min} - G_0}{k_B T} \right) + 1 \right\} \tag{19}$$

with the minimum energy given by Eq. (18) and the concentration-dependent part of the local chemical potential

$$G_0 = k_B T \log\left(\frac{c_0}{1 - c_0} \right). \tag{20}$$

Obviously, if $W_{\min} - G_0 \gg k_B T > 0$ and $0 < c_0 \ll 1$, as for high temperatures and dilute solutions, Eq. (19) simplifies to the Boltzmann distribution,

$$c_{\max} \approx c_0 \exp\left(-\frac{W_{\min}}{k_B T} \right). \tag{21}$$

Fig. 7 shows the maximum fractional hydrogen concentration near the tips of a microcrack, according to Eq. (19), as a function of the plate half-thickness, in the case of steel and tantalum, respectively, at two extreme temperatures and for two extreme values of the transfer length; conditions already envisaged for the numerical determination of the fractional hydrogen background concentration in the centre of the plate. We note that, apart from discernible deviations at high values of concentration, the curves essentially resemble those of Fig. 3, with the maximum hydrogen concentration exceeding the hydrogen background concentration by about 1.5–5 times, the effect being most pronounced at the lower temperature and for the smaller value of the transfer length. The variation of the relative maximum enhancement of the hydrogen concentration with the uniaxial tensile flow stress, calculated from Eq. (19), is displayed in Fig. 8, again in the case of steel and tantalum, respectively, at the same temperatures and for the same values of the transfer length, addressing two extreme values of the half-thickness of the plate. This

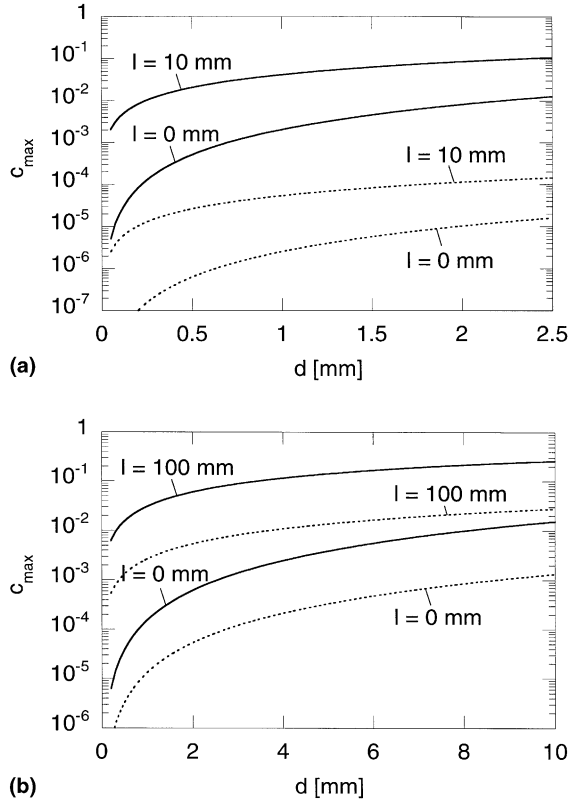

Fig. 7. Maximum fractional hydrogen concentration near the tips of a microcrack in the centre of a plate, $c_{\max}$, as a function of the plate half-thickness d, at a temperature ϑ of 100°C (full lines) and 300°C (dotted lines) for two different values of the transfer length l identified on the curves, in the case of (a) steel and (b) tantalum, obtained using the data in Table 1.

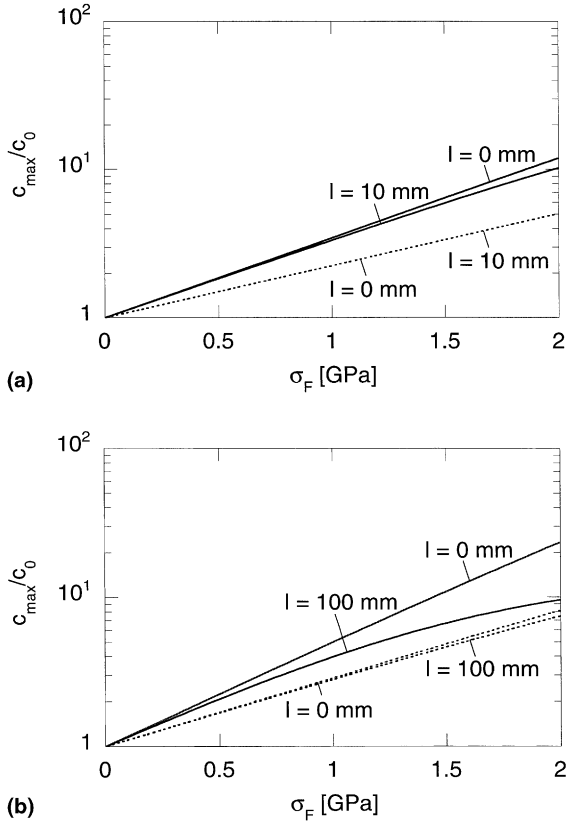

Fig. 8. Relative maximum enhancement of the fractional hydrogen concentration, $c_{\max}/c_0$, as a function of the uniaxial tensile flow stress σ_F, at a temperature ϑ of 100°C (full lines) and 300°C (dotted lines) for two different values of the transfer length l identified on the curves, in the case of (a) steel for a plate of half-thickness $d = 1$ mm and (b) tantalum for a plate of half-thickness $d = 10$ mm, obtained using the data in Table 1.

reveals an increase of the hydrogen concentration near the crack-tips of about 5–25 times the hydrogen background concentration; as in Fig. 7, the effect is most distinct at the lower temperature and for the smaller value of the transfer length. The deviations of the curves from straight lines, which are particularly noticeable at the lower temperature and for the higher value of the transfer length, reflect the influence of a strong mean occupancy of the available lattice sites, leading to a departure from the exponential law, Eq. (21).

We comment that, with the interaction energy, Eq. (17), and for the conditions underlying Eq. (21), the local hydrogen equilibrium concentration in the entire near-field region *outside* the plastic zone around the (right) crack-tip varies according to

$$c_e(r,\theta) \approx c_0 \exp\left(\sqrt{\frac{L}{r}}\cos\frac{\theta}{2}\right), \tag{22}$$

and hence decays away from the crack-tip on a length scale given by

$$L = \frac{2}{9\pi}\left((1+\nu)\frac{K_I \Delta V}{k_B T}\right)^2. \tag{23}$$

Like the lateral extent of the plastic zone, Eq. (15), does the decay length, Eq. (23), depend on the stress-intensity factor, Eq. (12), and therefore on the partial pressure of the internal hydrogen atmosphere, p_{int}. The latter quantity can be estimated by solving Eqs. (8) and (9) with Eq. (4) for $p = p_{int}$, assuming $\bar{c}_e = c_0$ at each given temperature. Numerical data of the hydrogen partial pressure and of these characteristic lengths are listed in Table 2, in the case of steel and tantalum, respectively, for two extreme temperatures and two extreme values of the transfer length, addressing two extreme values of the half-thickness of the plate and two representative values of the external tensile stress. In the case of steel the partial pressure developed by the internal hydrogen atmosphere is so high compared with the external tensile stress, that it gives rise to a significant enhancement of both characteristic lengths, particularly at the lower temperature, whereas in the case of tantalum it is so low compared with the external tensile stress, that it has very little effect on the characteristic lengths at all temperatures. Suffices it to add that the calculations underlying these predictions satisfy the conditions for both small-scale yielding of the elastic/ideally plastic continuum and for exponential decay of the hydrogen equilibrium concentration outside the crack-tip plastic zone.

5. Discussion and conclusions

Aiming to assess the implications of hydrogen effects for the performance and lifetime of materials in the target region of ESS, we compare the fractional hydrogen background concentration, c_0, and the maximum fractional hydrogen concentration near the tips of microcracks, c_{max}, predicted by our analysis for components in the form of plates with the respective critical concentration c^* giving rise to material degradation. For designers of spallation targets, embrittlement represents the most relevant type of degradation. Since a discussion of the complex variety of all forms of hydrogen embrittlement [40] is beyond the scope of our investigation, we refer to a recent compilation [41] which, in the case of the 9–12 at.% chromium steels favoured as structural materials for the target components of ESS, yields a mean critical fractional hydrogen concentration of $c_m^* \approx 5 \times 10^{-4}$.

The steel components most sensitive to hydrogen effects are the proton beam window and, for a liquid mercury target, also the window region of the return hull [2]. These double-walled structures are subject to the highest average hydrogen production rate per atom and pulsing cycle, $P \approx 9 \times 10^{-9}$ s^{-1}; as they must be

Table 2
Partial pressure of a hydrogen atmosphere inside the crack, together with characteristic lengths (relative to the crack half-length) of the plastic zone and the hydrogen concentration profile around it

ϑ (°C)	l (mm)	p_{int} (Pa)	r_p^*/a	L/a
(a) *Steel*[a]				
100	0	1.28×10^8	7.835×10^{-3}	7.745×10^{-3}
	10	9.26×10^8	1.593×10^{-1}	1.575×10^{-1}
300	0	2.30×10^4	2.292×10^{-3}	6.338×10^{-4}
	10	9.99×10^6	2.772×10^{-3}	7.665×10^{-4}
(b) *Tantalum*[b]				
100	0	3.97×10^{-1}	1.687×10^{-4}	4.218×10^{-4}
	100	1.75×10^2	1.687×10^{-4}	4.218×10^{-4}
300	0	1.92×10^1	3.306×10^{-4}	1.787×10^{-4}
	100	8.47×10^3	3.307×10^{-4}	1.788×10^{-4}

[a] For a plate of half-thickness $d = 1$ mm and the external tensile stress $\sigma_{ext} = 100$ MPa [39], obtained using the data in Table 1(a).
[b] For a plate of half-thickness $d = 10$ mm and the external tensile stress $\sigma_{ext} = 60$ MPa [3], obtained using the data in Table 1(b).

water-cooled, their mean temperature will be around 100°C. Similar conditions apply to the container of a solid target made up of water-cooled tantalum plates. According to the present design, the half-thickness of such window components will be $d = 1$ mm, or slightly less. Under these circumstances and for 'clean' surfaces, Fig. 3(a) anticipates a fractional hydrogen background concentration $c_0 \approx 8 \times 10^{-4}$, and Fig. 7(a) suggests a locally increased fractional hydrogen concentration $c_{max} \approx 2 \times 10^{-3}$ near the tips of microcracks. Both values which, following Fig. 4(a), will be reached within a period of less than 1 day, are already distinctly above the mean critical level $c_m^* \approx 5 \times 10^{-4}$. Surface barriers, considered in Figs. 3(a) and 7(a) too, and the possible contact with hydrogen in the state of H, H^+ or H_2^+, will further aggravate the situation. Although the concentration values quoted here merely represent estimates, the above comments clearly indicate that the use of ferritic/martensitic steels for water-cooled windows in ESS targets may well be problematic.

Obvious alternative materials for the proton beam window and the return hull appear to be austenitic stainless steels which are known as considerably less susceptible to degradation by hydrogen than ferrictic/martensitic steels [40]. Whether this benefit will be outweighed by the higher steady-state average hydrogen concentrations expected on account of the lower diffusivities of the hydrogen isotopes in austenites [42] is, however, an open question. The inferior strength (in the solution-annealed state) and inferior thermal conductivity of austenites does not seem to present a problem, since preliminary estimates show that the stresses (which will be mainly due to temperature gradients arising from the power deposition of the proton beam) shall stay well below the yield stresses of these materials. Another reason for the preference originally given to ferritic/martensitic, rather than to austenitic steels derives from the suspected stronger embrittlement of austenites by helium which, together with hydrogen, will also be produced at high rates in the environment of ESS (cf. Fig. 1 and the considerations in Section 2). Recent experimental results, however, indicate that for temperatures below 300°C, the observed hardening in both martensitic and austenitic steels arises predominantly from displacement-induced defects, whereas helium only plays an insignificant role up to fractional concentrations of 5×10^{-3} at least [43]. A final point in favour of austenites is their superior resistance against aqueous corrosion.

The situation, however, differs for the liquid mercury container: (i) the mean temperature in the beam entrance region will be around 300°C, or slightly below, and hence the fractional hydrogen background concentration, c_0, from Fig. 3(a), as well as the locally increased fractional hydrogen concentration near the tips of microcracks, c_{max}, from Fig. 7(a), will be down to levels safely below the mean critical level $c_m^* \approx 5 \times 10^{-4}$; (ii) the container walls are in contact with purified mercury (inside) and pure helium gas (outside), rendering the formation of surface barriers unlikely; (iii) the absence of water precludes aqueous corrosion and additional hydrogen loading by an influx of hydrogen in atomic or ionized form; (iv) in addition to the stresses arising from temperature gradients through heat deposition, the liquid mercury container walls will be subject to stresses caused by static and dynamic hydraulic forces as well as by pressure waves originating in the liquid [2,5] such that the total stress may exceed the design stresses of solution-annealed austenites; (v) ferritic/martensitic steels exhibit a lower corrosion rate in mercury than austenitic steels [44]. All these reasons make ferritic/martensitic steels a good choice for the liquid mercury container.

Tantalum as a prospective material for the solid target option of ESS does not seem to suffer from hydrogen degradation. In metals like titanium, zirconium and tantalum, hydride formation is generally considered to be the main cause for hydrogen-induced embrittlement effects. Fortunately, the solubility of hydrogen isotopes in tantalum is very high: $c_s^* > 1.5 \times 10^{-1}$ at room temperature already [45]. According to Figs. 3(b) and 7(b), neither the fractional hydrogen background concentration, c_0, nor the locally increased fractional hydrogen concentration near the tips of microcracks, c_{max}, is likely to attain such a high level in tantalum plates with a half-thickness between $d = 1$ and 5 mm, as envisaged in a preliminary design [2], even for almost impermeable surfaces at an operating temperature around 100°C. On the other hand, as Fig. 5(b) recommends, care should be taken that the external hydrogen partial pressure, p_{ext}, stays below the value of about 1 Pa, corresponding to the threshold hydrogen partial pressure p_{ext}^* above which the thermal equilibrium concentration of dissolved hydrogen, $\bar{c}_e$, exceeds the irradiation-induced hydrogen concentration, c_0. In practice, this condition appears to be safely fulfilled, since no hydrogen degradation has been observed in the water-cooled tantalum plates of a target, even after several years of non-continuous operation, in the 160 kW spallation source ISIS at the Rutherford–Appleton Laboratory [46], resulting in an accumulated displacement dose of about 10 dpa; a dose expected to accrue during 2 months of continuous full-power operation of ESS. It is interesting to note that the situation is much less favourable for zirconium and its alloys which show considerably lower hydrogen solubilities and diffusivities than does tantalum. A preliminary analysis indicates that, even for the reduced average hydrogen production rate per atom and pulsing cycle $P \approx 4 \times 10^{-9}$ s^{-1} in the Swiss 900 kW spallation source SINQ, the hydrogen solubility limit of its target rods will be reached already after a few hours of full-power operation. Embrittlement effects are, however, not expected in the presence of

hydrides with a volume fraction below about 5×10^{-2} [39], as for several months of continuous full-power operation.

The results of our study and the preceding discussion suggest the following conclusions.

1. The maximum fractional hydrogen concentration near the tips of microcracks in steel or tantalum plates subject to the conditions of ESS can exceed the fractional hydrogen background concentration by many times.
2. For operating temperatures around 100°C, as applying to the water-cooled proton windows and the return hull of ESS, transmutation-produced hydrogen isotopes may lead to severe degradation of the mechanical properties of ferritic/martensitic steels.
3. No hydrogen degradation of ferritic/martensitic steels is anticipated for the liquid mercury container of ESS, whose highly loaded regions will operate at a mean temperature around 300°C, or slightly below.
4. No hydrogen embrittlement due to hydride formation is expected for plates made of tantalum as a prospective material for the solid target option of ESS.

Further investigations are necessary in order to resolve whether austenitic steels are suitable alternative materials to ferritic/martensitic steels.

Acknowledgements

We thank Professor K. Schroeder, Dr H. Trinkaus and Professor H. Wipf for valuable discussions and useful comments.

References

[1] H. Lengeler, in: Proc. 13th Meeting of International Collaboration on Advanced Neutron Sources, PSI Report, Villingen, 1995, p. 819.
[2] J. Kjems, in: A New Generation Neutron Source for Europe, vol. III, ESS Technical Study, Roskilde, 1997, p. 4.
[3] H. Ullmaier, F. Carsughi, Nucl. Instrum. and Meth. B 101 (1995) 406.
[4] H. Ullmaier, H. Trinkaus, Mater. Sci. Forum 97–99 (1992) 451.
[5] L.K. Mansur, H. Ullmaier (Eds.), Proc. Int. Workshop on Spallation Materials Technology, ORNL Report, Oak Ridge, TN, 1996.
[6] J.P. Hirth, B. Carnahan, Acta Metall. 26 (1978) 1795.
[7] J.P. Hirth, Metall. Trans. 11A (1980) 861.
[8] R. Kirchheim, J.P. Hirth, Scr. Metall. 16 (1982) 475.
[9] J.P. Hirth, in: R.A. Oriani, J.P. Hirth, M. Smialowski (Eds.), Hydrogen Degradation of Ferrous Alloys, Noyes, Park Ridge, NJ, 1985, p. 131.
[10] H. Rauh, R. Bullough, Proc. R. Soc. London A 397 (1985) 121.
[11] H. Rauh, R. Bullough, Proc. R. Soc. London A 427 (1990) 1.
[12] H. Rauh, in: K.P. Herrmann, Z.S. Olesiak (Eds.), Thermal Effects in Fracture of Multiphase Materials, Springer, Berlin, 1990, p. 46.
[13] D. Filges, R.D. Neef, H. Schaal, A. Tietze, U. Weber, W. Breuer, J. Wimmer (Eds.), Damage Studies for Structure and Beam Window Materials for the ESS Mercury Target, ESS Report, Jülich, 1996.
[14] S.L. Green, W.V. Green, F.H. Hegedüs, M. Victoria, W.F. Sommer, B.M. Oliver, J. Nucl. Mater. 155–157 (1988) 1350.
[15] D. Filges, C. Mayer, R.D. Neef, H. Schaal, A. Tietze, J. Wimmer (Eds.), Development of Cross Sections for Materials Damage and Helium Production for ESS, ESS Report, Jülich, 1996.
[16] K. Schroeder, Z. Phys. B 25 (1976) 91.
[17] F. Wedig, P. Jung, J. Nucl. Mater. 245 (1997) 138.
[18] K.S. Forcey, I. Iordanova, M. Yaneva, J. Nucl. Mater. 240 (1997) 118.
[19] G. Schaumann, J. Völkl, G. Alefeld, Phys. Status Solidi 42 (1970) 401.
[20] T. Heumann, in: Diffusion in Metallen, Springer, Berlin, 1992, p. 220.
[21] H. Rauh, R. Bullough, J.R. Matthews, Philos. Mag. A 65 (1992) 53.
[22] J.D. Hobson, J. Iron Steel Inst. 191 (1959) 342.
[23] R. Boler, C.B.A. Forty, G.J. Butterworth, in: An Initial Examination of the Likely Effect of Hydrogen on Low Activation Martensitic Steel, AEA Report, Culham, 1992, p. 3.
[24] M.P. Puls, in: R.A. Oriani, J.P. Hirth, M. Smialowski (Eds.), Hydrogen Degradation of Ferrous Alloys, Noyes, Park Ridge, NJ, 1985, p. 114.
[25] T. McMullen, M.J. Stott, E. Zaremba, Philos. Mag. A 59 (1989) 161.
[26] T. Schober, H. Wenzl, in: G. Alefeld, J. Völkl (Eds.), Hydrogen in Metals II, Springer, Berlin, 1978, p. 11.
[27] T. Schober, C. Dieker, R. Feenstra, J. Phys. F 18 (1988) 1119.
[28] H. Rauh, R. Bullough, M.H. Wood, Proc. R. Soc. London A 388 (1983) 311.
[29] H.P. van Leeuwen, in: R.A. Oriani, J.P. Hirth, M. Smialowski (Eds.), Hydrogen Degradation of Ferrous Alloys, Noyes, Park Ridge, NJ, 1985, p. 16.
[30] H. Borchers, H. Hausen, K.H. Hellwege, K. Schäfer, E. Schmidt (Eds.), Landolt-Börnstein, Zahlenwerte und Funktionen aus Physik, Chemie, Astronomie, Geophysik und Technik, N.S., vol. II/1, Springer, Berlin, 1971, p. 298.
[31] J.A. Beattie, O.C. Bridgeman, Proc. Am. Acad. Arts Sci. 63 (1928) 299.
[32] R.R. Heinrich, C.E. Johnson, C.E. Crouthamel, J. Electrochem. Soc. 112 (1965) 1067.
[33] I. Ali-Khan, K.J. Dietz, F. Waelbroeck, P. Wienhold, J. Nucl. Mater. 74 (1978) 132and138.
[34] D. Broek, in: Elementary Engineering Fracture Mechanics, Kluwer Academic, Dordrecht, 1991, p. 94.
[35] D. Gross, in: Bruchmechanik, Springer, Berlin, 1996, p. 96.
[36] G. Leibfried, N. Breuer, Point Defects in Metals I, Springer, Berlin, 1978, pp. 189 and 227.
[37] A. Magerl, B. Berre, G. Alefeld, Phys. Status Solidi (a) 36 (1976) 161.

[38] A.P. Sutton, R.W. Balluffi, in: Interfaces in Crystalline Materials, Clarendon, Oxford, 1995, p. 436.
[39] J.B. Bai, C. Prioul, D. François, Metall. Trans. 25A (1994) 1185.
[40] H.G. Nelson, in: M.R. Louthan, R.P. McNitt, R.D. Sisson (Eds.), Proc. Conf. on Environmental Degradation of Engineering Materials, vol. III, Pennsylvania State University, University Park, PA, 1987, p. 83.
[41] P. Jung, Fus. Technol. 33 (1998) 63.
[42] K.S. Forcey, D.K. Ross, J.C.B. Simpson, D.S. Evans, J. Nucl. Mater. 160 (1988) 117.
[43] H. Ullmaier, E. Camus, J. Nucl. Mater. 251 (1997) 262.
[44] J.F. Nejedlik, E.J. Vargo, Corrosion 20 (1964) 250.
[45] T. Schober, in: F.A. Lewis, A. Aladjem (Eds.), Hydrogen Metal Systems I, Scitec, Uetikon, 1996, pp. 357 and 423.
[46] T. Broome, private communication.